589950

# Micro-pulse Lidar Signals: Uncertainty Analysis

*Submission to Journal of Atmospheric and Oceanic Technology: Notes and Correspondence*

Ellsworth J. Welton[1] and James R. Campbell[2]

1. Goddard Earth Sciences and Technology Center
University of Maryland Baltimore County
Baltimore, Maryland 21250 USA
Ph: 301-614-6279
Fax: 301-614-5492
Email: welton@virl.gsfc.nasa.gov

2. Science Systems and Applications, Inc.
Lanham, Maryland 20706 USA
Ph: 301-614-6273
Fax: 301-614-5492
Email: campbell@virl.gsfc.nasa.gov

Dec 19, 2001
Submitted Version
EJW

589950

December 20, 2001

# Micro-pulse Lidar Signals: Uncertainty Analysis

Authors:
Ellsworth J. Welton* and James R. Campbell

*Submission to the Journal of Atmospheric and Oceanic Technology*

Micro-pulse lidar (MPL) systems are small, autonomous, eye-safe lidars used for continuous observations of the vertical distribution of cloud and aerosol layers. Since the construction of the first MPL in 1993, procedures have been developed to correct for various instrument effects present in MPL signals. The primary instrument effects include afterpulse, laser-detector cross-talk, and overlap, poor near-range (< 6 km) focusing. The accurate correction of both afterpulse and overlap effects are required to study both clouds and aerosols. Furthermore, the outgoing energy of the laser pulses and the statistical uncertainty of the MPL detector must also be correctly determined in order to assess the accuracy of MPL observations.

The MPL-Net project at GSFC coordinates the deployment of MPL instruments to sites co-located with AERONET sunphotometers. The raw MPL data is downloaded to a central archive and processed to correct for the various instrument effects discussed above. A paper that describes the techniques used to correct the raw MPL data has been accepted for publication by the Journal of Atmospheric and Oceanic Technology. However, the paper did not discuss the net uncertainty in the corrected MPL-Net data product.

This new paper discusses the uncertainties in the determination of the afterpulse, overlap, pulse energy, detector noise, and all remaining quantities affecting measured MPL signals. The uncertainties are propagated through the entire correction process to give a net uncertainty on the final corrected MPL-Net data product. The results show that in the near range, the overlap uncertainty dominates. At altitudes above the overlap region, the dominant source of uncertainty is caused by uncertainty in the pulse energy. However, if the laser energy is low, then during mid-day, high solar background levels can significantly reduce the signal-to-noise of the detector. In such a case, the statistical uncertainty of the detector count rate becomes dominant at altitudes above the overlap region.

* Lead Author: Dr. Ellsworth J. Welton
Goddard Earth Sciences and Technology Center, UMBC
GSFC Code 912
welton@virl.gsfc.nasa.gov

## Abstract

Micro-pulse lidar (MPL) systems are small, autonomous, eye-safe lidars used for continuous observations of the vertical distribution of cloud and aerosol layers. Since the construction of the first MPL in 1993, procedures have been developed to correct for various instrument effects present in MPL signals. The primary instrument effects include afterpulse, laser-detector cross-talk, and overlap, poor near-range (< 6 km) focusing. The accurate correction of both afterpulse and overlap effects are required to study both clouds and aerosols. Furthermore, the outgoing energy of the laser pulses and the statistical uncertainty of the MPL detector must also be correctly determined in order to assess the accuracy of MPL observations. The uncertainties associated with the afterpulse, overlap, pulse energy, detector noise, and all remaining quantities affecting measured MPL signals, are determined in this study. The uncertainties are propagated through the entire MPL correction process to give a net uncertainty on the final corrected MPL signal. The results show that in the near range, the overlap uncertainty dominates. At altitudes above the overlap region, the dominant source of uncertainty is caused by uncertainty in the pulse energy. However, if the laser energy is low, then during mid-day, high solar background levels can significantly reduce the signal-to-noise of the detector. In such a case, the statistical uncertainty of the detector count rate becomes dominant at altitudes above the overlap region.

## 1. Introduction

During the 1990s technological advances made possible the development of compact, autonomous, and eye-safe lidar systems. The Micro-pulse Lidar (MPL) was the first of this new class of instruments (Spinhirne, 1993; Spinhirne et al., 1995). The MPL has since been used successfully within the Atmospheric Radiation Measurement (ARM) program (Stokes and Schwartz 1994), and also in several independent field experiments around the world (Welton et al., 2000; Peppler et al., 2000; Voss et al., 2001; Welton et al., 2001). An overview of the MPL instruments operated within the ARM program is discussed by Campbell et al. (2001), henceforth referred to as CA.

Welton et al. (2000) and CA discuss the nature of the measured MPL signal with respect to the lidar equation (Fernald et al., 1972). The measured signals are shown to differ from the theoretical lidar equation because of specific effects caused by the MPL transmit/receive optical design. Both Welton et al. and CA develop correction factors for each instrument-related effect, and present algorithms that convert the measured signal into a form that complies with the lidar equation.

The two algorithms differ in their approach to the correction process. The earlier algorithm by Welton et al. determined the correction factors by forcing measured signals to conform to a modeled lidar signal containing only molecular scattering. However, this method is only useful when measurements can be conducted in regions free of aerosols and clouds, such as on mountain-tops. The CA algorithm is not dependent upon this condition, and is more applicable to most field conditions. Also, the CA algorithm is more rigorous in its construction, and is better suited to understanding the uncertainties involved in the correction process. For these reasons, an adapted version of the CA algorithm was used by Welton et al. (2001) for

processing MPL data from a later field experiment. The authors intend to utilize the CA algorithm for future studies.

This paper presents a study of the uncertainties associated with the correction factors discussed by CA. The uncertainties are propagated through the CA algorithm to yield a net uncertainty in the final converted MPL signal.

## 2. The MPL Signal

This section describes the terms that are present in the lidar equation. Figure 1 shows an example of MPL observed photon count rates during both day and night. The MPL count rate is presented as Equation 2 in CA, and is rewritten here as

$$P_{raw}(r) = \frac{CE\,O(r)\left[\beta_M(r) + \beta_P(r)\right] T_M^{\,2}(r)\, T_P^{\,2}(r)}{D(P_{raw})\, r^2} + \frac{A_{raw}(r,E)}{D(P_{raw})} + \frac{B_{raw}}{D(P_{raw})} \qquad (1)$$

where $P_{raw}(r)$ is the measured signal (photoelectrons/μsec per shot) at range $r$, $C$ is a calibration value, $E$ is the pulse energy in μJ, $D(P_{raw})$ is the detector dead-time factor, $O(r)$ is the overlap function, $A(r,E)$ is the detector afterpulse (photoelectrons/μsec per shot), and $B$ is the solar background signal (photoelectrons/μsec per shot).

**Normalized Relative Backscatter Signals**

The backscatter cross-section terms, $\beta_M(r)$ and $\beta_P(r)$, in Eq. (1) are due to molecules and particles, respectively. Sources of particle backscatter include clouds, aerosols, or a mixture of both. The transmission terms, $T_M^2(r)$ and $T_P^2(r)$, are given by

$$T_i^2(r) = \exp\left[-2\int_0^r \sigma_i(r')dr'\right] \tag{2}$$

where $\sigma(r)$ is the extinction coefficient, and the $i$ subscript denotes either a molecular or particle quantity. The integral of the extinction coefficient from the MPL to any range is the optical depth over that distance. The transmission terms are squared to account for the two-way path of the laser pulses.

The aim of the CA correction algorithm is to remove all instrument parameters from Eq. (1) except $C$, and to subtract $B$. The signal resulting from the correction process is called the normalized-relative-backscatter signal, henceforth referred to as the NRB signal. The NRB signal, $P_{NRB}(r)$, is given by

$$P_{NRB}(r) = C\left[\beta_M(r) + \beta_P(r)\right]T_M^2(r)T_P^2(r) \tag{3}$$

The NRB signal is significant because it is dependent on atmospheric parameters and only one instrument parameter, $C$. Techniques to determine $C$ using measured NRB signals are well understood and are independent of the lidar system (Spinhirne et al.,1980; Welton et al., 2001).

**Detector Dead-time Corrections**

The first step in processing the MPL signals is to correct for detector dead-time effects. Dead-time effects are caused by saturation of the detector signals at high count rates and are discussed in detail by CA. Here we attempt to quantify the uncertainty in the dead-time correction based on information provided by the manufacturer and others with expertise in the field of photon counting detectors (X. Sun, personal communication).

The dead-time factor is determined using the following equation,

$$D(P_{raw}) = \frac{\chi}{P_{raw} A} \tag{4}$$

where $\chi$ is a calibrated source signal, $A$ is the total attenuation of the optical path from the source to the detector, and $P_{raw}$ is the observed photon count rate. The uncertainty in $D(P_{raw})$ is given by,

$$\delta D(P_{raw}) = D(P_{raw}) \sqrt{\left(\frac{\delta\chi}{\chi}\right)^2 + \left(\frac{\delta A}{A}\right)^2 + \left(\frac{\delta P_{raw}}{P_{raw}}\right)^2} \tag{5}$$

where $\delta\chi$ and $\delta P_{raw}$ are the uncertainties in the source and measured signals, respectively, and are determined using Poisson statistics. $\delta A$ is the uncertainty in the attenuation term. The uncertainties in each signal term are estimated assuming a per second count rate with no time average. The source uncertainty was well below 1% and was negligible. The attenuation uncertainty was ignored in order to assess the uncertainty in the dead-time caused by fluctuations in the source and measured signal.

Figure 2a shows a plot of $D(P_{raw})$ versus the measured count rate, $P_{raw}$. Figure 2b shows $\delta D(P_{raw})/D(P_{raw})$ versus $D(P_{raw})$. The dead-time uncertainty is negligible at high count rates but approaches 1% at low count rates because the detector uncertainty is highest when the count rate is low. However, the dead-time factor itself is only significant for values above 1.01, the level at which the measured signals are affected by at least 1% due to dead-time effects. At dead-time factors above 1.01, the dead-time uncertainty is less than 0.3%. As a result, the source and measured signal uncertainties contribute very little to the overall dead-time uncertainty. Instead, the uncertainty in the dead-time factor is dependent almost entirely on the uncertainty in the

attenuation optic. The attenuation uncertainty is not know at this time. For the purposes of this study, we will consider this to be small and the overall dead-time uncertainty to be negligible.

The dead-time corrected lidar signal, P($r$), is given by

$$\mathrm{P}(r) = \frac{E\mathrm{O}(r)\mathrm{P}_{\mathrm{NRB}}(r)}{r^2} + \mathrm{A}(r,E) + B \tag{6}$$

Using Poisson statistics, the uncertainty in P($r$) is

$$\delta\mathrm{P}(r) = \sqrt{\frac{\mathrm{P}(r)}{N}} \tag{7}$$

where $N$ is the number of shots during the acquisition of the signal and is dependent on the data rate. $N$ is typically either 75,000 for a 30 second data rate, or 150,000 for a 1 minute data rate. Figure 1 shows the uncertainty in the observed count rate. Also, the error in $B$ is given by Eq. (7), but is done using the signal returns from 45 to 55 km as discussed by CA.

**Uncertainties in the Laser Energy**

A portion of the outgoing laser pulse energy is measured in real-time by another detector, the energy monitor. A calibration table is used to calculate the actual pulse energy from the energy monitor value. The relationship between the two is linear. The calibration table does not have to be very accurate in terms of generating the true output energy. Instead, it only has to provide an output energy that is proportional to the actual value because any constant offset in the energy term can be passed to the calibration value, $C$. Henceforth, the term energy monitor value refers to the calibrated pulse energy, not the actual pulse energy.

The average energy monitor value during the measurement period (typically 1 minute) is stored in the MPL data file. Changes in the energy monitor value from pulse to pulse during the measurement period will produce uncertainty in the energy value. If the energy uncertainty becomes high it can dominate the uncertainty in the MPL signal. Therefore, the energy monitor value must be carefully considered.

The energy monitor value can change from pulse to pulse due to changes in the laser power setting, degradation of the laser diode over time, changes in beam quality output from the laser head, and statistical fluctuations in the energy monitor. The laser power setting is fixed during operation of the MPL. Therefore, the diode power will only drop if the laser system begins to degrade, however this takes place over a long time span and will not produce pulse to pulse changes in the energy unless a catastrophic failure occurs. The laser head components may also degrade with time, but again this will not produce significant pulse to pulse changes unless the laser head breaks. The beam quality may be affected by environmental changes such as increase or decrease in temperature and humidity of the laser components. This could occur over much smaller time frames and is considered a possible source of uncertainty. Statistical fluctuations in the energy monitor are also considered a source of uncertainty. In addition, temperature changes on the energy monitor produce another source of uncertainty because of thermal noise in the detector.

The uncertainty in the energy monitor value was determined using the following procedure. Data from five MPL systems were collected. Table 1 shows the average energy, percent energy fluctuation, average temperature, and percent temperature fluctuation of each MPL system over M number of minutes of data. The energy monitor values range from 3.71 to 7.64 μJ and the temperature values range from 26.93° to 30.55° C between the MPL systems

picked for this study. MPL systems have varying degrees of laser quality due to age, and this range of energy covers the typical span found in most MPL systems. Also, the temperature range covers the typical span encountered during most MPL operations. Figure 3 shows the percent fluctuation in energy versus the percent fluctuation in temperature for the five MPL systems. The data show that when the change in temperature is low, the percent fluctuation in the energy monitor value is approximately 1% or less. When the change in temperature is low, the primary source of energy change is simply statistical fluctuation within the detector. Typical MPL data acquisition rates are 1 minute or less and temperature changes are negligible over such short time spans unless there is a noticeable problem with the instrument. Therefore, under normal conditions the uncertainty in the energy monitor value is set constant to 1% for all MPL systems. However, if the data rate is increased to several minutes or more, then temperature fluctuations affecting the energy uncertainty should be considered.

## 3. Afterpulse Corrections

The next step in MPL processing is the afterpulse correction. A complete discussion of afterpulse is given by CA, a brief description is given here. The initial firing of each laser pulse is seen by the detector because the MPL shares the same transmit and receive path. The initial pulse on the detector is large and creates a false signal on the detector as the photoelectrons are bled off. This false signal must be removed from the measured signals by pre-determining $A(r,E)$, and then subtracting it from $P(r)$. This process is referred to as afterpulse correction and is discussed here. $A(r,E)$ is determined by covering the MPL and preventing signals from being transmitted. In this arrangement, the first term on the right-hand-side (RHS) of Eq. (6) is zero, and the detector only measures the afterpulse signal and background. The background is only

equal to the detector dark noise with the lid on. The afterpulse is dependent upon the output energy and according to CA is written as

$$A(r, E_A) = E_A A_N(r) \tag{8}$$

where $E_A$ is the energy monitor value during the afterpulse measurement.

$A_N(r)$ is referred to as the normalized afterpulse. In order to measure $A_N(r)$, the dark noise is subtracted from $P(r)$ and the result is divided by $E_A$. $A_N(r)$ is given by

$$A_N(r) = \frac{A(r)}{E_A} = \frac{P(r) - B_D}{E_A} \tag{9}$$

where $B_D$ is the detector dark noise. This measurement is performed for a certain period of time (typically about 10 minutes). $A_N(r)$ is the average of the signals over the time span, and the afterpulse uncertainty, $\delta A(r)$, is

$$\delta A_N(r) = A_N(r) \sqrt{\frac{\delta P(r)^2}{[P(r) - B]^2} + \left(\frac{\delta E_A}{E_A}\right)^2} \tag{10}$$

where $\delta E_A$ is the uncertainty in the outgoing energy during the afterpulse measurement. Figure 4a shows a typical afterpulse function versus range, and Figure 4b shows the afterpulse uncertainty.

Signals measured during regular operations are corrected by subtracting $EA_N(r)$ from $[P(r)-B]$ and then dividing by $E$. However, $B$ and $E$ are the values taken during the regular

measurement, not the afterpulse measurement. The normalized-afterpulse-corrected signal, $P_{NA}(r)$, is given by

$$P_{NA}(r) = \frac{P(r) - B - [E A_N(r)]}{E} = \frac{O(r) P_{NRB}(r)}{r^2} \tag{11}$$

## 4. Overlap Corrections

The next step in MPL processing is the overlap correction. A complete discussion of overlap is given by CA, a brief description is given here. The overlap function accounts for signal loss in the near-range due to poor receiver efficiency of the telescope and associated optics in this region. The overlap problem must be corrected in order to analyze boundary layer aerosols. The CA overlap correction process involves acquiring MPL data while the instrument is oriented horizontally. In this arrangement, both $\beta$ and $\sigma$ are constant with range. Using Eq. (3) and multiplying Eq. (11) by $r^2$ gives the resulting horizontal MPL signal

$$P_H(r) = C\beta O(r) \exp[-2\sigma r] \tag{12}$$

The natural logarithm of Eq. (12) is

$$\ln[P_H(r)] = \ln[C\beta] + \ln[O(r)] - 2\sigma r \tag{13}$$

At distances greater than the overlap range, $O(r)$ is equal to one and the second term on the RHS of Eq. (13) is zero. In this region, $\ln[P_{NA}(r)]$ is linear with respect to range. A least squares linear

fit is applied to $N$ data points from $r_O$ to a maximum range, $r_{max}$. The maximum range is typically about 2 km greater than $r_O$. The resulting linear fit is given by

$$\ln[P_F(r)] = \ln[C\beta] - 2\sigma r \tag{14}$$

where the y-intercept is $\ln[C\beta]$ and the slope is $-2\sigma$. The overlap function is calculated using the following equation

$$O(r) = \begin{cases} \dfrac{P_H(r)}{P_F(r)} & r < r_O \\ 1 & r \geq r_O \end{cases} \tag{15}$$

where $P_F(r)$ is simply the exponential of the fit line (and is equal to $P_{NRB}(r)$). The uncertainty in the overlap is given by

$$\delta O(r) = O(r)\sqrt{\left[\frac{\delta P_H(r)}{P_H(r)}\right]^2 + \left[\frac{\delta P_F(r)}{P_F(r)}\right]^2} \tag{16}$$

The first term under the square root in Eq. (16) is uncertainty in the signal, and is given by

$$\left[\frac{\delta P_H(r)}{P_H(r)}\right]^2 = \frac{[\delta P(r)]^2 + \delta B^2 + [A_N(r)\delta E_O]^2 + [E_O \delta A_N(r)]^2}{[P(r) - B - E_O A_N(r)]^2} + \left[\frac{\delta E_O}{E_O}\right]^2 \tag{17}$$

where $E_O$ is the energy monitor value during the overlap measurement. The second term under the square root in Eq. (16) is uncertainty due to the fit process and is given by

$$\left[\frac{\delta \mathrm{P_F}(r)}{\mathrm{P_F}(r)}\right]^2 = \left[\frac{\delta(C\beta)}{C\beta}\right]^2 + \left[\frac{\delta(\exp[-2\sigma r])}{\exp[-2\sigma r]}\right]^2 \tag{18}$$

The fit uncertainty is a function of the uncertainties in both the y-intercept and slope obtained during the fit. Standard error analysis is used to determine the uncertainties for both parameters. First we define the following terms

$$\Omega = X\sum_{i=1}^{X} r_i^2 - \left(\sum_{i=1}^{X} r_i\right)^2 \tag{19}$$

and

$$s^2 = \frac{1}{X-2}\sum_{i=1}^{X}\left(\ln[\mathrm{P_{NA}}(r)] - \ln[\mathrm{P_F}(r)]\right)^2 \tag{20}$$

The uncertainty in the y-intercept is then given by

$$\delta(\ln[C\beta]) = \sqrt{\frac{s^2}{\Omega}\sum_{i=1}^{X} r_i^2} \tag{21}$$

and the uncertainty in the slope is

$$\delta(-2\sigma) = \sqrt{X\frac{s^2}{\Omega}} \tag{22}$$

The results of Eq. (21) and Eq. (22) are then used to determine the uncertainty terms on the RHS of Eq. (18). The equations are given by

$$\frac{\delta(C\beta)}{C\beta} = \frac{\left[\left(e^{\ln[C\beta]+\delta(\ln[C\beta])} - e^{\ln[C\beta]}\right) + \left(e^{\ln[C\beta]} - e^{\ln[C\beta]-\delta(\ln[C\beta])}\right)\right]}{2e^{\ln[C\beta]}} \tag{23}$$

and

$$\frac{\delta(\exp[-2\sigma r])}{\exp[-2\sigma r]} = r\delta(-2\sigma) \tag{24}$$

The final overlap uncertainty is calculated using Eq. (16). Figure 5 shows a typical overlap function and its uncertainty.

Signals measured during regular operations are overlap corrected by dividing $P_{NA}(r)$, Eq. (11), by the pre-determined overlap, $O(r)$. The resulting signal is termed the normalized-afterpulse-overlap-corrected signal, $P_{NAO}(r)$, and is given by

$$P_{NAO}(r) = \frac{\dfrac{P(r) - B - [E A_N(r)]}{E}}{O(r)} = \frac{P_{NRB}(r)}{r^2} \tag{25}$$

## 5. Normalized Relative Backscatter Signals

$P_{NAO}(r)$ is simply the NRB signal divided by the range squared. The final step in the MPL processing is to multiply $P_{NAO}(r)$ by $r^2$. The result is the NRB signal and is given by

$$P_{NRB}(r) = r^2 P_{NAO}(r) = \frac{r^2\left[\frac{P(r) - B - [E A_N(r)]}{E}\right]}{O(r)} \tag{26}$$

The uncertainty in the NRB signal is given by

$$\delta P_{NRB}(r) = P_{NRB}(r)\sqrt{\frac{[\delta P(r)]^2 + \delta B^2 + [A_N(r)\delta E]^2 + [E\delta A_N(r)]^2}{[P(r) - B - E A_N(r)]^2} + \left[\frac{\delta E}{E}\right]^2 + \left[\frac{\delta O(r)}{O(r)}\right]^2} \tag{27}$$

Figure 6a shows the NRB signal generated from the measured daytime signal in Figure 1. Figure 6b shows the uncertainty in the daytime NRB values. Figures 6c and 6d show the night-time NRB signal and its uncertainty for comparison. The night-time uncertainties are decreased because of the lack of solar background, $B$.

## 6. Conclusion

Figure 7 displays NRB signals, and uncertainties, obtained during one full-day. The boundary layer and two cirrus layers are both visible in the image. The reduction in NRB uncertainty at high altitudes during the night is clearly shown. Also, the ability of the MPL to

detect the presence of moderate to thick cirrus layers at one-minute data rate during mid-day (low signal-to-noise) is shown. During mid-day, NRB signal uncertainties in clear air regions approach 100% at approximately 6 km. However, when cirrus is encountered the NRB signal uncertainties drop considerably due to an increase in the signal-to-noise within the cloud. However, detecting thin cirrus during daytime at one-minute data rates is difficult. This problem can be overcome by averaging NRB signals over several minute periods.

In general, near the surface, the overlap uncertainty is the dominant source of uncertainty in the NRB signal. At altitudes above the overlap region, the dominant source of uncertainty in the NRB signal is typically due to uncertainty in the energy. However, during daytime $B$ increases and reduces the signal-to-noise, which causes $\delta P_{NRB}(r)$ to increase accordingly. Therefore, during the daytime $B$ is also a large source of uncertainty at higher altitudes.

## Acknowledgements

This work was conducted by members of the MPL-Net project at NASA Goddard Space Flight Center. The MPL-Net project is funded by the NASA Earth Observing System and the SIMBIOS project. The authors thank Stan Scott, Tim Berkoff, Matt McGill, Dennis Hlavka, Bill Hart, Jim Spinhirne, and Xiaoli Sun for helpful discussions on the matter of uncertainties in the various MPL components.

## References

Campbell, J. R., D. L. Hlavka, E. J. Welton, C. J. Flynn, D. D. Turner, J. D. Spinhirne, V. S. Scott, and I. H. Hwang, 2001: Full-time, Eye-Safe Cloud and Aerosol Lidar Observation at Atmospheric Radiation Measurement Program Sites: Instrument and Data Processing. *J. Atmos. Oceanic Technol.*, accepted.

Fernald, F. G., B. M. Herman, and J. A. Reagan, 1972: Determination of aerosol height distributions by lidar, J. Appl. Meteorol., **11**, 482-489.

Peppler, R. A., C. P. Bahrmann, J. C. Barnard, J. R. Campbell, M. D. Cheng, R. A. Ferrare, R. N. Halthore, L. A. Heilman, D. L. Hlavka, N. S. Laulainen, C. J. Lin, J. A. Ogren, M. R. Poellot, L. A. Remer, K. Sassen, J. D. Spinhirne, M. E. Splitt, and D. D. Turner, 2000: ARM Southern Great Plains Site Observations of the Smoke Pall Associated with the 1998 Central American Fires. *Bull. Amer. Meteor. Soc.*, **81**, 2563-2591.

Sasano, Y., H. Shimizu, N. Takeuchi, and M. Okuda, 1979: Geometrical form factor in the laser radar equation: an experimental determination. Appl. Opt., **18**, 3908-3910.

Spinhirne, J. D., J. A. Reagan, and B. M. Herman, 1980: Vertical Distribution of Aerosol Extinction Cross Section and Inference of Aerosol Imaginary Index in the Troposphere by Lidar Technique. *J. Appl. Meteorol.*, ***19***, 426-438.

Spinhirne, J. D., 1993: Micro Pulse Lidar. *IEEE Trans. Geosci. Remote Sens.*, **31**, 48-55.

Spinhirne, J. D., J. A. R. Rall, and V. S. Scott, 1995: Compact Eye Safe Lidar Systems. *Rev. Laser Eng.*, **23**, 112-118.

Stokes, G. M., and S. E. Schwartz, 1994: The Atmospheric Radiation Measurement (ARM) Program: Programmatic background and design of the cloud and radiation testbed. *Bull. Amer. Meteorol. Soc.*, **75**, 1201-1221.

Voss, K. J., E. J. Welton, P. K. Quinn, J. Johnson, A. Thompson, and H. Gordon, 2001: Lidar Measurements During Aerosols99. *J. Geophys. Res.*, **106**, 20821-20832.

Welton, E. J., K. J. Voss, H. R. Gordon, H. Maring, A. Smirnov, B. Holben, B. Schmid, J. M. Livingston, P. B. Russell, P. A. Durkee, P. Formenti, M. O. Andreae, 2000: Ground-based Lidar Measurements of Aerosols During ACE-2: Instrument Description, Results, and Comparisons with other Ground-based and Airborne Measurements. *Tellus B*, **52**, 635-650.

Welton, E. J., K. J. Voss, P. K. Quinn, P. J. Flatau, K. Markowicz, J. R. Campbell, J. D. Spinhirne, H. R. Gordon, and J. E. Johnson, 2001: Measurements of aerosol vertical profiles and optical properties during INDOEX 1999 using micro-pulse lidars. *J. Geophys. Res.*, in press.

## Figure Captions

Figure 1. Example of MPL observed count rates (a). The uncertainty in the observed count rate using Poisson statistics (b). Both day and night observations are shown.

Figure 2. The detector dead-time factor versus measured count rates (a). The fractional percent uncertainty in the dead-time factor (b). The dead-time factor is only significant above 1.01, and the uncertainties are below 0.3%.

Figure 3. Percent fluctuation in energy monitor values versus the percent fluctuation in temperature for the five different MPL systems in Table 1.

Figure 4. A typical normalized afterpulse signal (a). The afterpulse percent uncertainty (b). The afterpulse uncertainty is dominated by the uncertainty in the energy monitor value.

Figure 5. A typical overlap function (a) and its fractional percent uncertainty (b).

Figure 6. The results of corrections to the day and night MPL count rates from Figure 1 are shown. The daytime NRB signal and uncertainty are shown in 6a and 6b, respectively. The night-time NRB signal and uncertainty are shown in 6c and 6d, respectively.

Figure 7. NRB signals obtained during a full day of MPL observations are shown in the upper panel. The bottom panel shows the NRB fractional percent uncertainty.

Table 1. Energy Uncertainty

| MPL # | Average Energy (μJ) | % Fluctuation in Energy | Average Temperature (C°) | % Fluctuation in Temperature | Samples (M) |
|---|---|---|---|---|---|
| 1 | 6.88 ± 0.07 | 1.00 | 26.93 ± 0.66 | 2.45 | 318 |
| 2 | 3.71 ± 0.03 | 0.85 | 27.77 ± 0.09 | 0.33 | 1423 |
| 3 | 6.60 ± 0.25 | 3.82 | 24.02 ± 1.75 | 7.28 | 2823 |
| 4 | 7.64 ± 0.12 | 1.57 | 30.55 ± 0.89 | 2.92 | 1272 |
| 5 | 3.82 ± 0.12 | 3.23 | 28.43 ± 1.69 | 5.93 | 1204 |

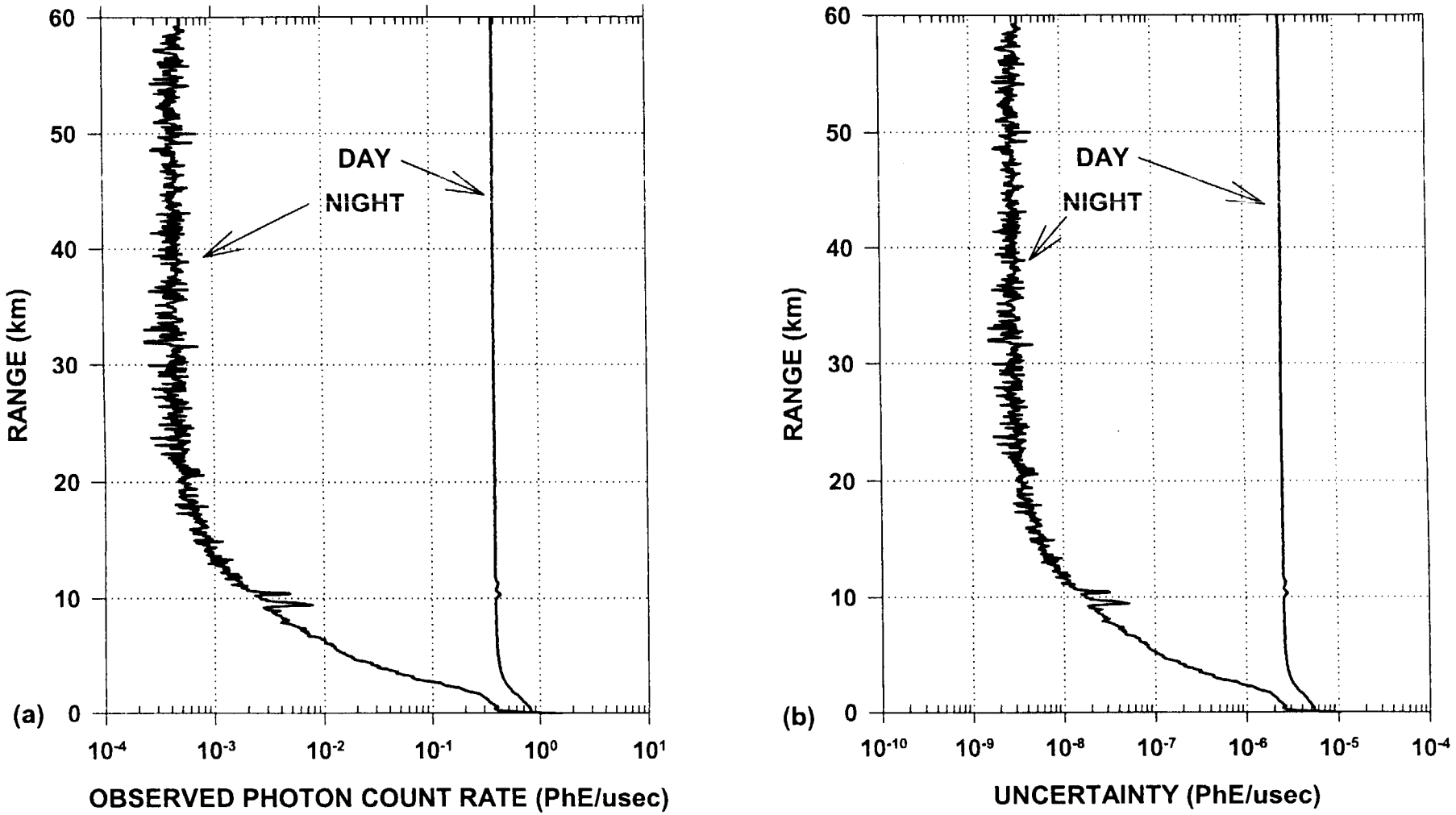
60
50
40
30
20
10
0
RANGE (km)
DAY
NIGHT
(a)
$10^{-4}$
$10^{-3}$
$10^{-2}$
$10^{-1}$
$10^{0}$
$10^{1}$
OBSERVED PHOTON COUNT RATE (PhE/usec)
(b)
$10^{-10}$
$10^{-9}$
$10^{-8}$
$10^{-7}$
$10^{-6}$
$10^{-5}$
$10^{-4}$
UNCERTAINTY (PhE/usec)

Figure 1

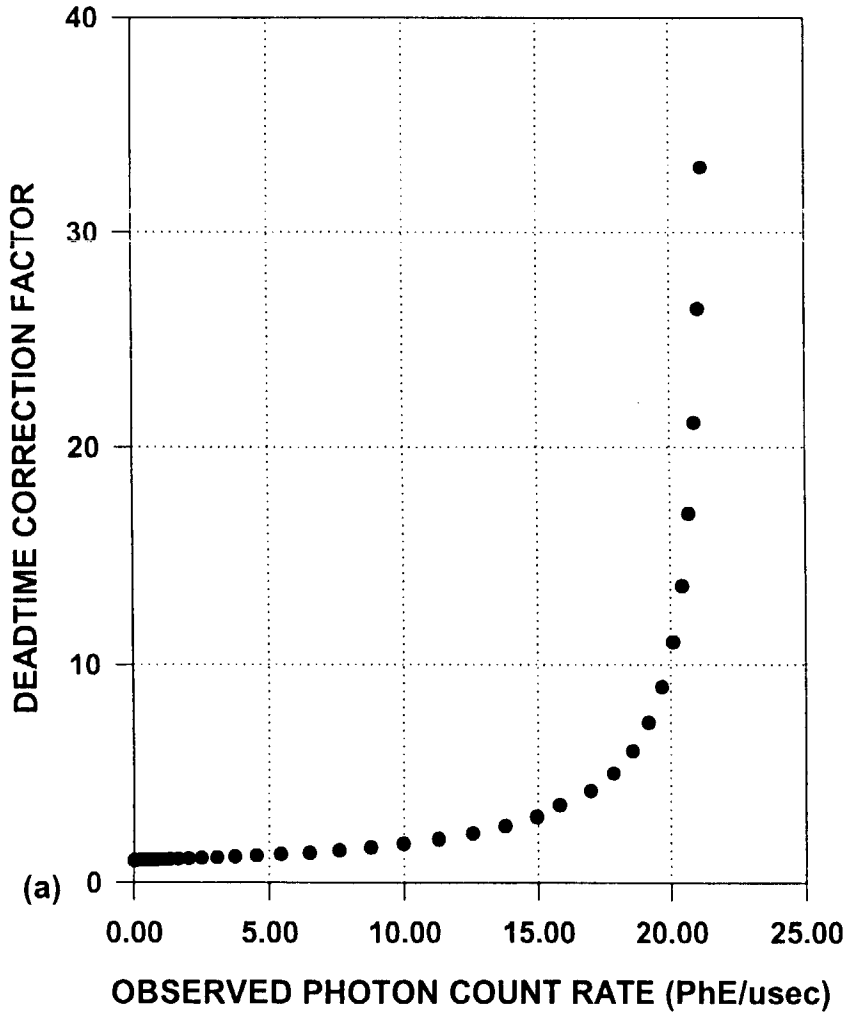
40
30
20
10
0
(a)
DEADTIME CORRECTION FACTOR
0.00
5.00
10.00
15.00
20.00
25.00
OBSERVED PHOTON COUNT RATE (PhE/usec)

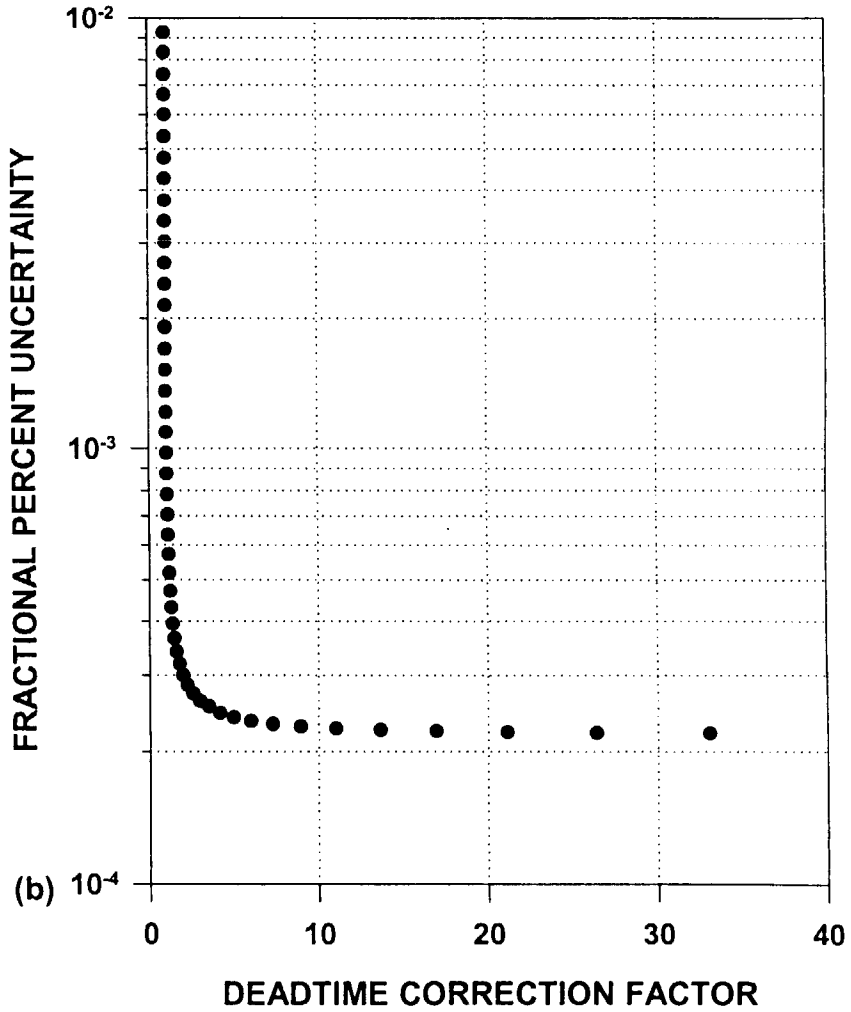
$10^{-2}$
$10^{-3}$
$10^{-4}$
(b)
FRACTIONAL PERCENT UNCERTAINTY
0
10
20
30
40
DEADTIME CORRECTION FACTOR

Figure 2

Figure 3

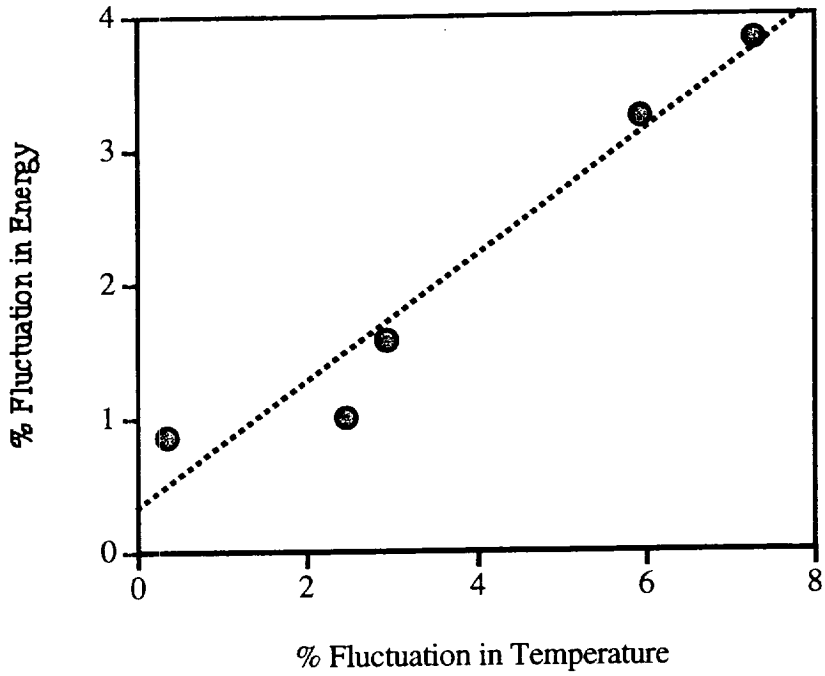
% Fluctuation in Energy
% Fluctuation in Temperature
0
1
2
3
4
0
2
4
6
8

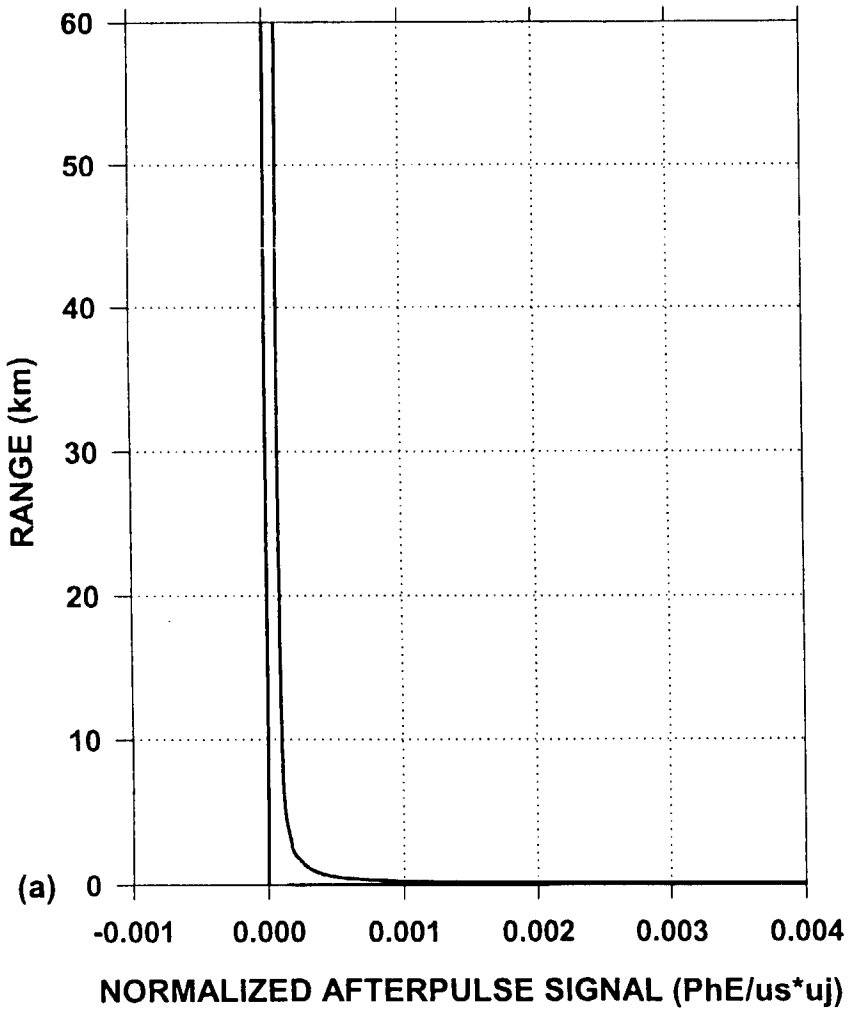
60
50
40
30
20
10
0
RANGE (km)
(a)
-0.001
0.000
0.001
0.002
0.003
0.004
NORMALIZED AFTERPULSE SIGNAL (PhE/us*uj)

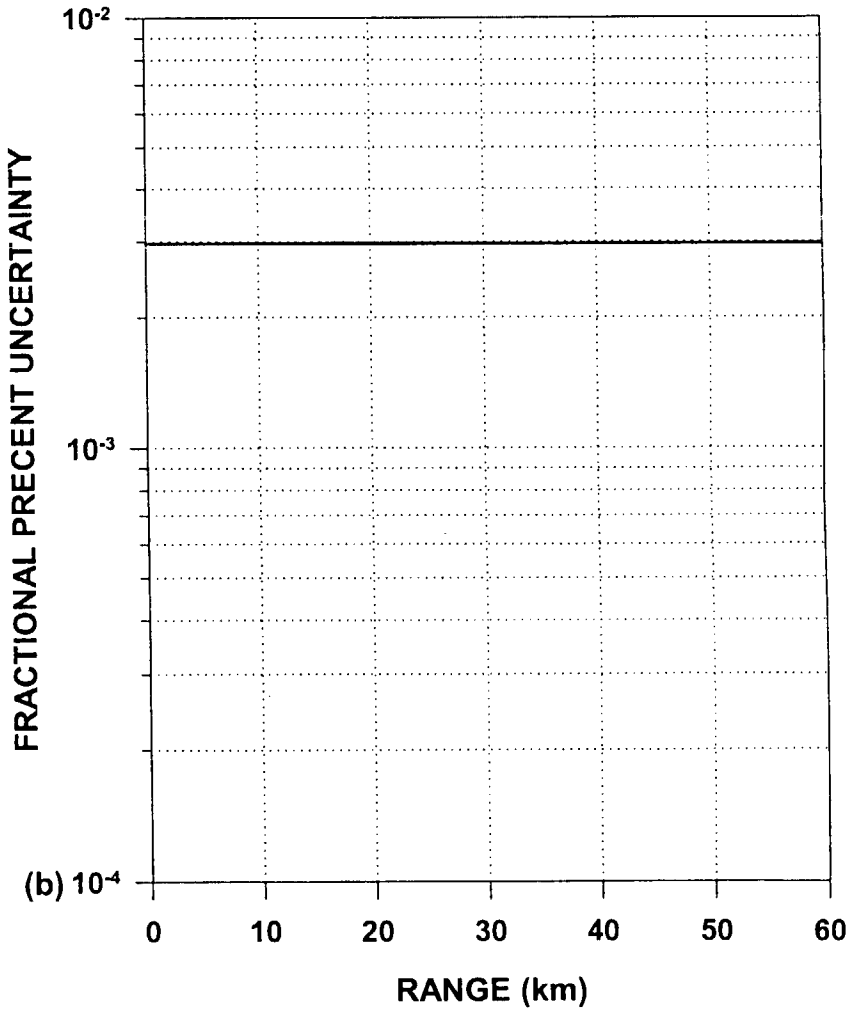
$10^{-2}$
$10^{-3}$
$10^{-4}$
FRACTIONAL PRECENT UNCERTAINTY
(b)
0
10
20
30
40
50
60
RANGE (km)

Figure 4

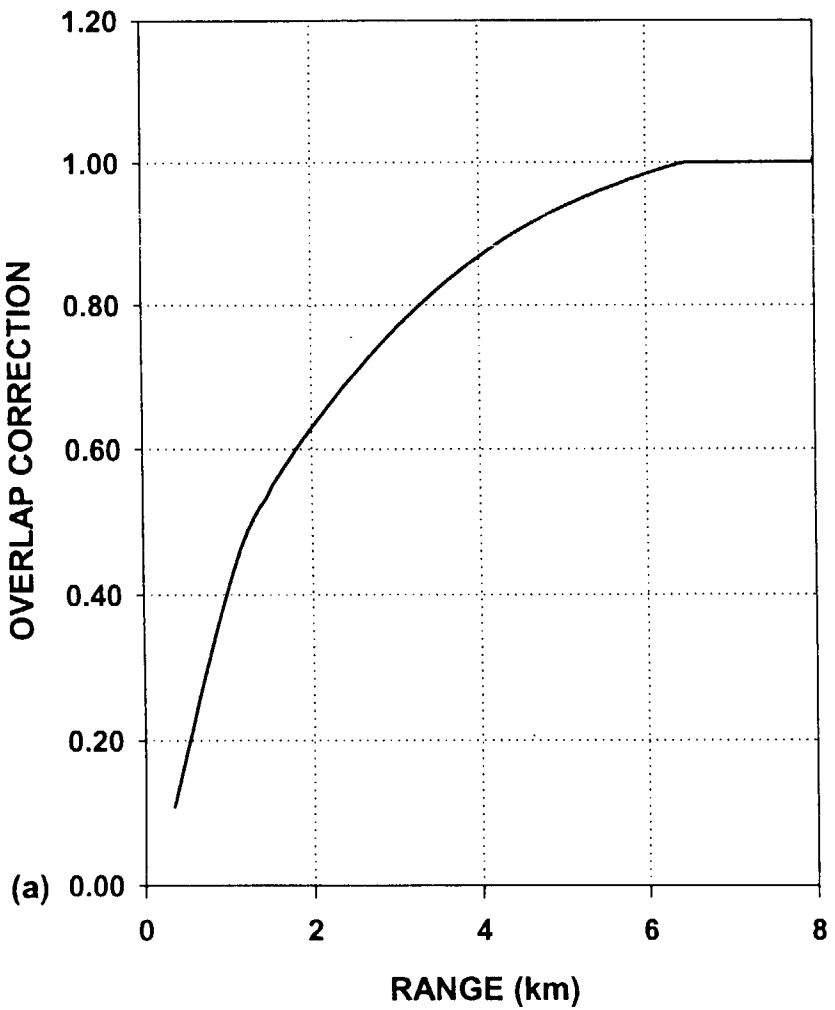
1.20
1.00
0.80
0.60
0.40
0.20
0.00
OVERLAP CORRECTION
(a)
0
2
4
6
8
RANGE (km)

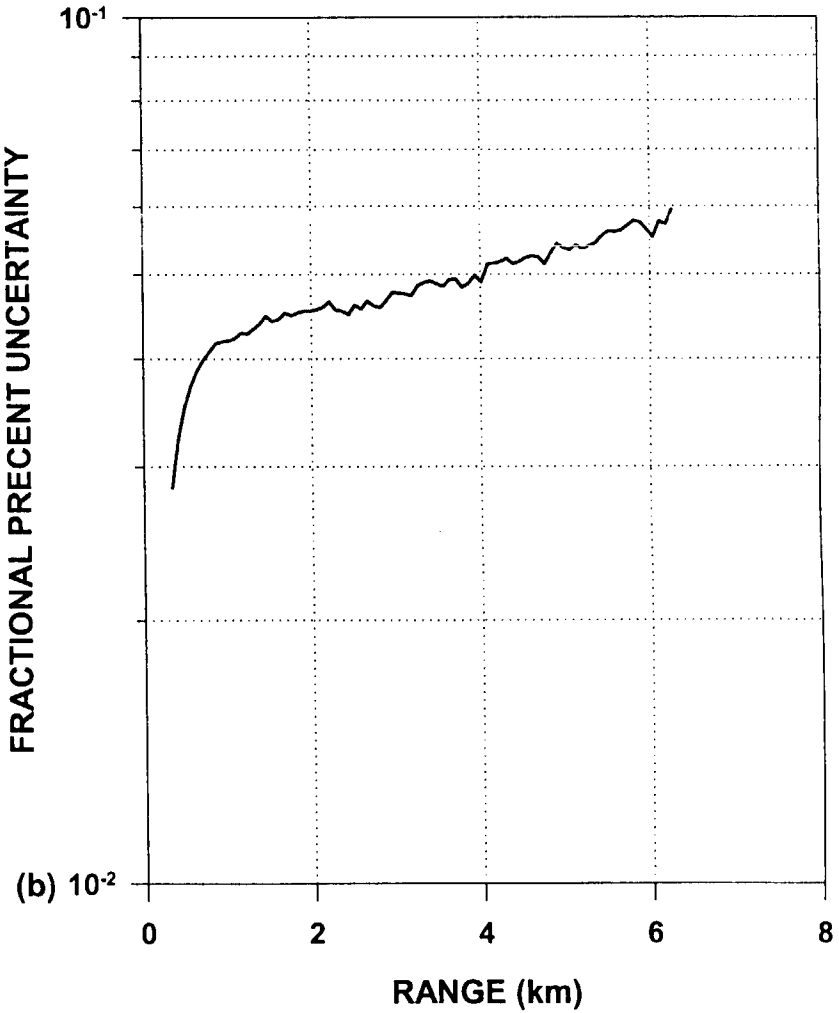
$10^{-1}$
FRACTIONAL PRECENT UNCERTAINTY
(b) $10^{-2}$
0
2
4
6
8
RANGE (km)

Figure 5

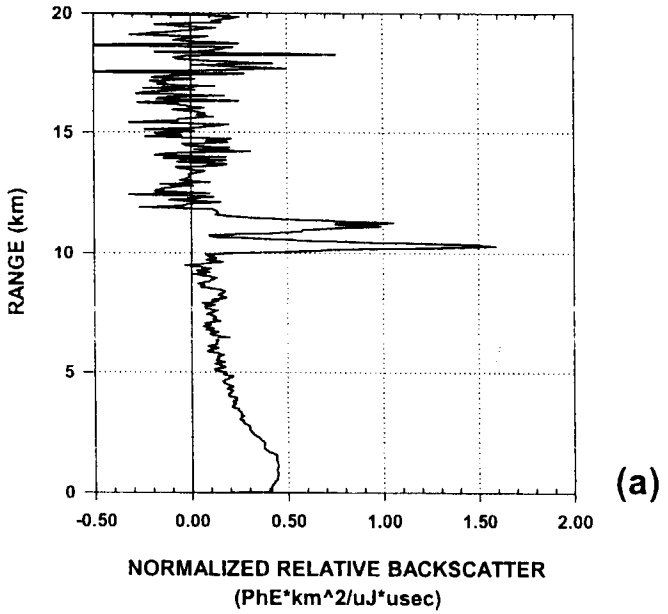


(a)

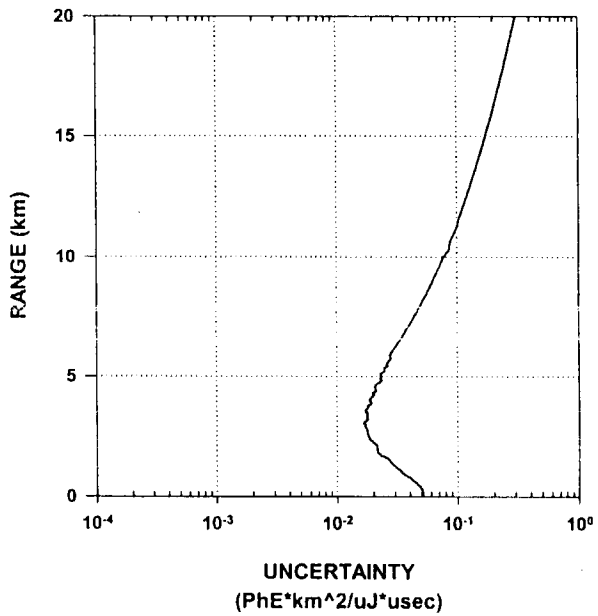


(b)

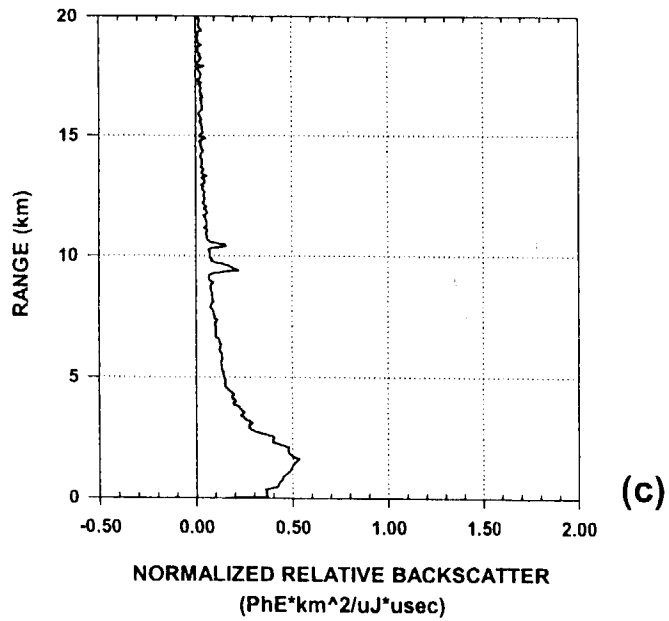


(c)

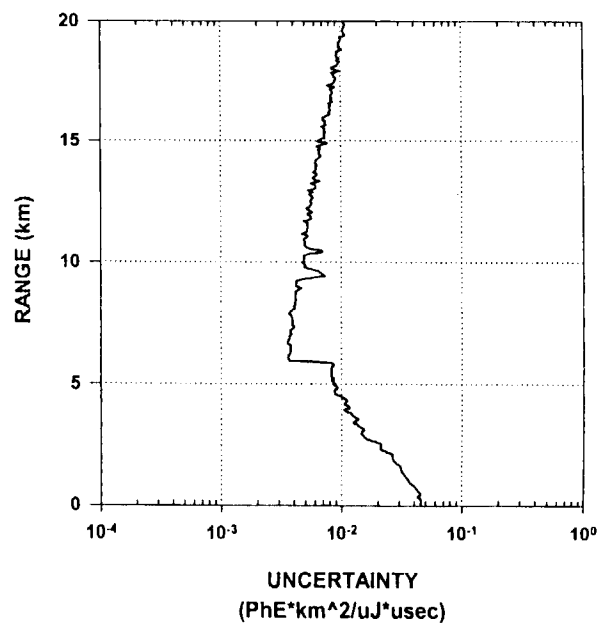


(d)

Figure 6

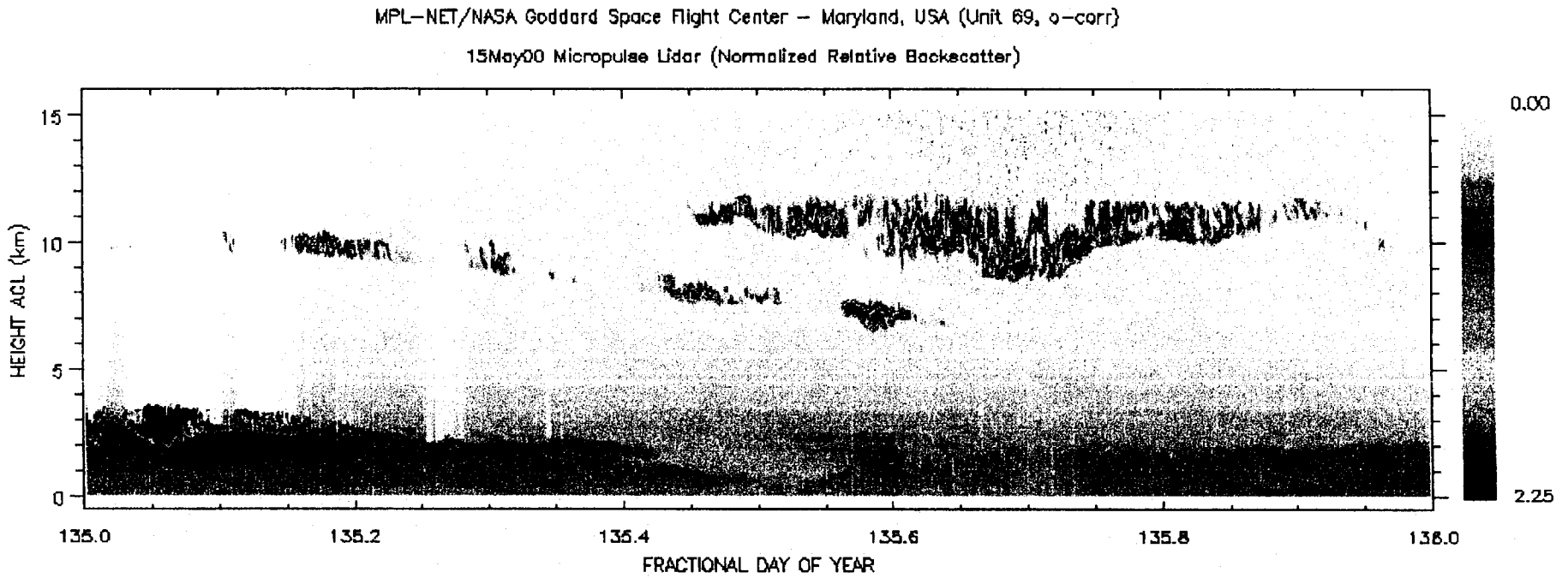
MPL-NET/NASA Goddard Space Flight Center - Maryland, USA (Unit 69, o-corr)
15May00 Micropulse Lidar (Normalized Relative Backscatter)
HEIGHT AGL (km)
0
5
10
15
135.0
135.2
135.4
135.6
135.8
136.0
FRACTIONAL DAY OF YEAR
0.00
2.25

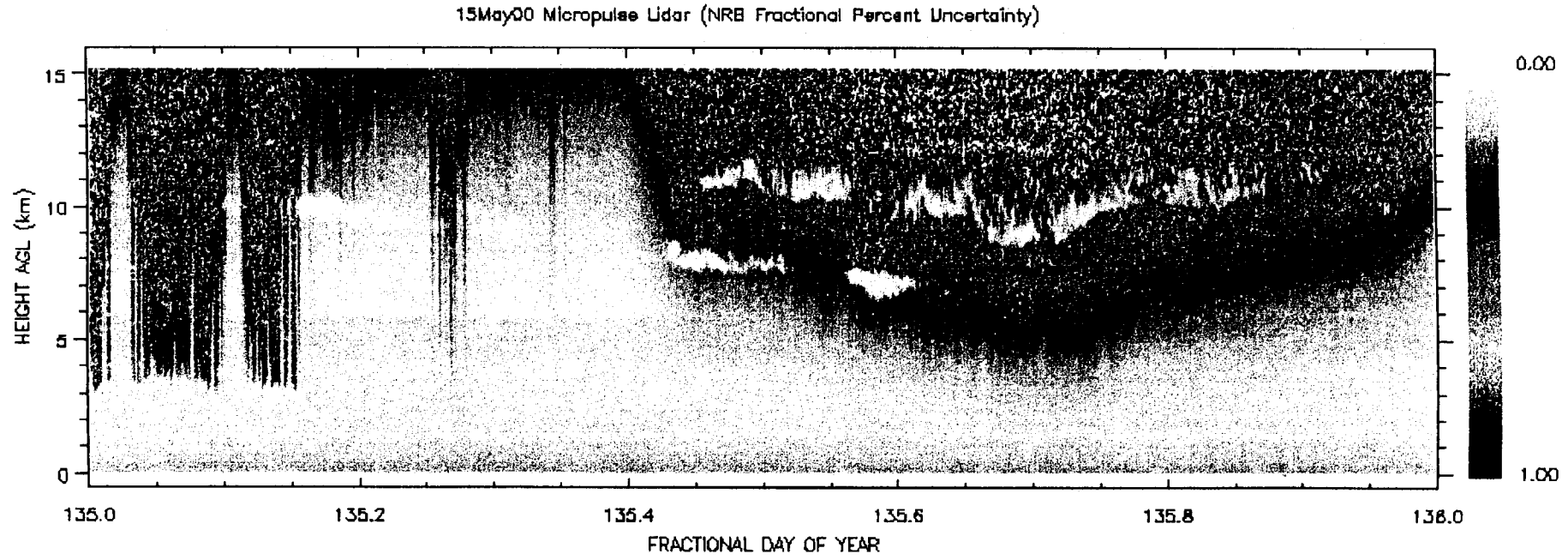
15May00 Micropulse Lidar (NRB Fractional Percent Uncertainty)
HEIGHT AGL (km)
0
5
10
15
135.0
135.2
135.4
135.6
135.8
136.0
FRACTIONAL DAY OF YEAR
0.00
1.00